

Numerical modeling of distributed combustion in a novel ultra-low emission turbulent swirl burner

Dániel Füzési^{a,*}, Milan Malý^b, Jan Jedelský^b, Viktor Józsa^a

^a Budapest University of Technology and Economics, Faculty of Mechanical Engineering, Department of Energy Engineering, H-1111 Budapest, Műegyetem rkp. 3., Hungary

^b Faculty of Mechanical Engineering, Brno University of Technology, Technická 2896/2, 616 69 Brno, Czech Republic

Abstract

Distributed combustion offers ultra-low NO_x emission, proven by several experimental works. The aim of this numerical study is to better understand the operation of such a combustion system, using a Mixture Temperature-Controlled burner. The most significant contribution of this paper is discussing a robust framework for distributed combustion modeling. Moreover, diesel fuel combustion was investigated, which is scarce in the public literature. In this paper, two operating conditions were presented at which distributed combustion was observed. The reacting flow was modeled by Flamelet-Generated Manifold, based on a detailed mechanism of n-dodecane, a single-component representative of diesel fuel. The Zimont model was used for the turbulent flame speed estimation with significantly reduced coefficients to achieve distributed combustion. The droplets of airblast atomization were tracked in a Lagrangian frame. The numerical results were validated by Schlieren images. The reactant dilution ratio remained below 0.25 through the combustion chamber, meaning that it is not the inner flue gas recirculation that leads to the favorable flame characteristics and excellent flame stability observed during the experiments. Both the measured and modeled NO_x emission was below 3 ppm.

Keywords: combustion; CFD; distributed; burner; swirl; liquid fuel

* Corresponding author. Email: fuzesi.daniel@gpk.bme.hu

1. Introduction

We live in the age of energy transition; the will to replace fossil fuels was never this strong. However, solving the 100 EJ problem [1] needs significantly more excess renewable energy to overcome. Consequently, liquid fuels will stay in the transportation sector for several decades [2]. To mitigate the consequences of the transition period, advanced fuels and novel technologies are needed [3]. Probably the most cumbersome branch of transportation to decarbonize is aviation, which has a separate, Sustainable Aviation Fuel (SAF) proposal in the European Union, called ReFuelEU [4], due to the lack of better feasible solution without severely compromising our current habits and needs. The reasons listed above strongly encourage the development of advanced combustion concepts and the clean operation of new and retrofitted systems, which is the principal motivation of the present paper.

The least advanced and currently developed combustion concept is the rich burn-quick quench-lean burn technology, used in most commercial aviation jet engines [5], which can utilize SAF. Lean swirl burners feature notably lower emissions but struggle with thermoacoustic problems at the design point [6]. Catalytic combustors were proposed to mitigate this problem but failed to have a market penetration due to excessive unburnt fuel emission [7]. Porous media burners are under development [8], but their disadvantage is the low turndown ratio, an important measure of the current heat engines. Several ongoing studies deal with flameless or Moderate or Intense, Low-oxygen Dilution (MILD) combustion to reduce the NO_x emission principally [9]. Kumar et al. [10] investigated kerosene combustion in a two-stage combustor with tangential air dilution achieving 75% NO_x drop at distributed mode. Gupta et al. [11] determined the Damköhler number of colorless distributed combustion in the order of magnitude of 10^{-2} , concluding that slow reactions characterize this regime. J. A. Wüning and J. G. Wüning [12] determined the exhaust gas recirculation limits of flameless combustion. The stable flameless mode can be achieved in a narrow, low recirculation rate

range and with high reactant rates, if the operating temperature is higher than the ignition temperature. Accordingly, a significant recirculation rate is needed to ensure distributed combustion [10,12]. However, the exhaust gas recirculation or inert gas dilution [13] for MILD combustion is not an option in, e.g., gas turbines.

To overcome this issue, the Mixture Temperature-Controlled (MTC) combustion concept was introduced [14], delivering ultra-low NO_x emissions and stable lean flame by using ambient air as an oxidizer. The essence of this novel concept is mixture cooling, which can be performed by, e.g., an airblast atomizer, ultimately delaying ignition and allowing more time for achieving homogeneous mixture and reduced volumetric Heat Release Rate (HRR). Consequently, distributed combustion can be realized without combustion air dilution.

The present paper aims to understand the operation of distributed combustion of the MTC concept via Computational Fluid Dynamics (CFD) simulations at two combustion setups. For validation, Schlieren measurements were performed. Following the preliminary investigations on diesel and waste cooking oil combustion [15], it was concluded that unsteady calculations are inevitable to model distributed combustion. A robust way to consider turbulence-chemistry interaction is using tabulated Flamelet Generated Manifold (FGM) [16]. Another implication is the modeling of the diesel fuel spray. The gas-phase was modeled in the Eulerian frame, while the Lagrangian frame was used for liquid fuel droplets, standard in both diesel engine [17] and jet engine [18] simulations. Reynolds-Averaged Navier-Stokes models can be applied for colorless distributed combustion modeling, focusing on hydrogen [19,20], which is not applicable in the present case. Highly simplified 2D biodiesel combustion modeling was performed in ref. [21], using the one-equation eddy dissipation model and steady calculations, which cannot be implemented in distributed combustion modeling. MILD combustion is highly relevant for industrial applications, such as biomass-fired utility boilers [22]. Validi et al. [23] used a complex Large Eddy Simulation (LES) model combined with

filtered mass density functions to simulate methane colorless distributed combustion. The LES results were compared to Particle Image Velocimetry (PIV) images, showing a poor match. V. K. Arghode et al. [24] performed steady-state colorless methane combustion simulation, validated by PIV measurements with a mixed agreement. Karyeyen et al. [20] validated their model under non-reacting conditions. Accordingly, both the simulation of distributed combustion and its validation is not fully resolved. The present paper principally aims to provide guidelines for distributed combustion simulation.

2. Materials and methods

This section starts with a brief introduction of the measurement setup, emphasizing the Schlieren technique, used principally for validation. Subsection 2.2 details the computational mesh and the numerical setup. Lastly, the fuel properties were detailed since the modeling of distributed combustion is sensitive to the material properties, requiring realistic thermophysical data besides detailed chemistry-based modeling.

2.1 Measurement setup

The geometry of the modeled burner is shown in Fig. 1. The airblast atomizer nozzle is blue, and the 45° flat swirl vanes are red with 40 mm tip and 21 mm hub diameters. The length of the mixing tube is 100 mm from the atomizer nozzle, directing the mixture into the combustion chamber. The yellow part is for gas/auxiliary air injection, which was not used this time.

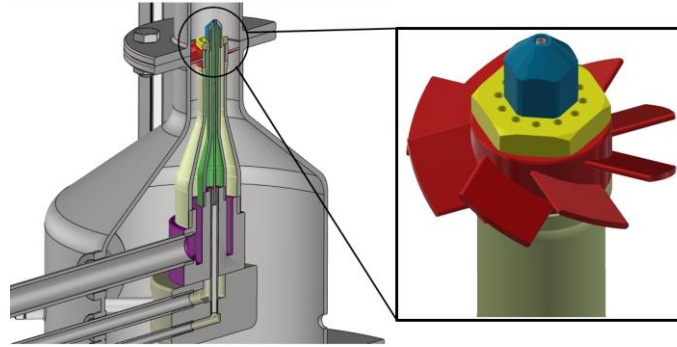


Fig. 1. The geometry of the modeled burner.

Figure 2 shows the schematic measurement setup, including the two-mirror Schlieren optical system, which provides line-of-sight information on refractive index variation. The mirror diameters were 150 mm with 750 mm focal length. The system directly provides qualitative density difference inside the area of interest. Image recording was performed at 10 kHz by a FASTCAM SA-Z type 2100K-M-16GB (Photron, Japan) for 0.2 s, acquiring a total of 2,000 images. The flame was illuminated by an HPLS-36DD18B (Lightspeed Technologies, USA) pulsed LED light source. The numerically investigated equivalence ratio (ϕ) was 0.57, while two atomizing gauge pressures (p_a) were used, 0.75 (Case 1) and 0.9 bar (Case 2). The elevated p_a was necessary to enter the distributed combustion regime [14]. The thermal power was 13.3 kW. All the other notable conditions required for modeling are discussed in Subsection 2.2.

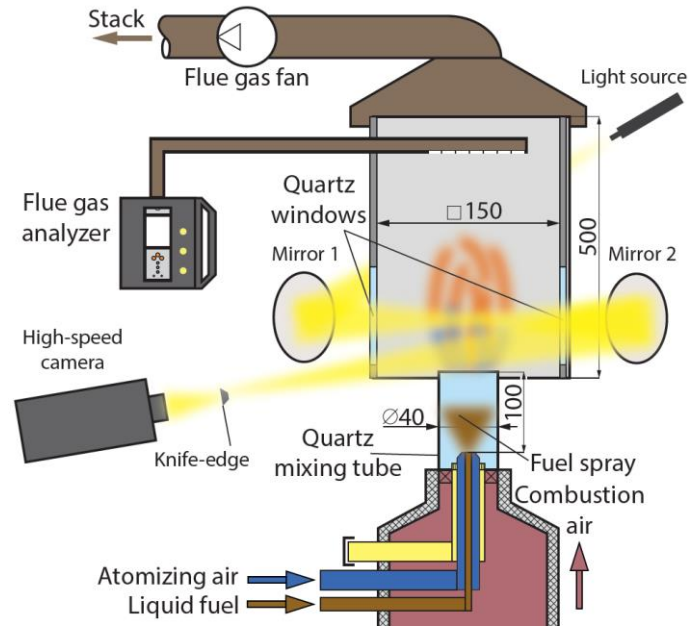


Fig. 2. Schematic of the combustion chamber with the Schlieren setup.

2.2 Numerical modeling

The mosaic poly-hexacore mesh of the burner head and the combustion chamber is shown in Fig. 3, considering the real geometry and the best practices [25]. A virtual convergent nozzle at the outlet was added to avoid backflow and loss of numerical stability. The first half of the combustion chamber features higher resolution since the observed flame is confined to this region. The final mesh consisted of 302985 cells, according to the mesh sensitivity analysis, considering temperature, velocity magnitude, OH intensity and droplet diameter distributions. The full numerical problem was fully solved in the ANSYS Fluent 2020 R1 software environment, including mesh creation.

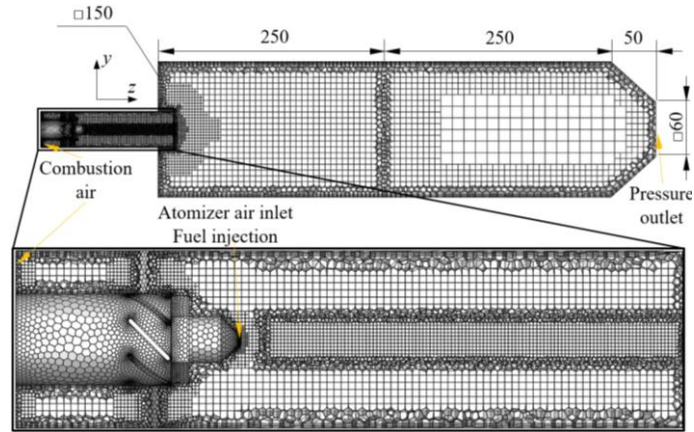


Fig. 3. Cross-section of the control volume (top), mesh of the burner/mixing tube (middle), and the burner lip (bottom, note the rotated view).

Spray modeling was included as a steady process to achieve better numerical stability that also comes with a notable reduction in computational cost. Consequently, breakup and coalescence were automatically neglected, which is justifiable in diluted sprays [26]. Atomization was modeled by the built-in airblast atomizer model with spray half-cone angle of 11° [27], fuel nozzle diameter of 0.9 mm, atomizer air annulus of 1.2 mm inner, and 2.2 mm outer diameter and liquid temperature of 25°C . The maximum relative inlet velocity was set according to the corresponding atomizer air inlet as 240 (Case 1) and 265 m/s (Case 2) [14]. Droplet motion was estimated by the discrete random walk and the random eddy lifetime stochastic models [28].

Diesel fuel was considered as 100% n-dodecane, similar to ref. [29], using the mechanism of the CRECK Modeling Group, including the thermochemical properties of the species [30]. The chemical reactions were considered by a thermochemical probability density function [28], using the FGM model. Combustion was modeled as partially premixed, using the *C* Equation [31], and the number of species was reduced to 15. For turbulence-chemistry interaction, the Zimont turbulent flame speed closure model was used, where the turbulent length scale and flame speed constants were set to 0.1, the Schmidt number to 1, and the wall

damping coefficient to 0.01. These uncommon parameter combinations were required to have distributed combustion instead of fast reactions and a straight flame, in line with the model description [28]. The laminar flame speed as a function of mean mixture fraction was imported from ref. [32]. Thermal radiation was considered by the discrete ordinates model, using the weighted-sum-of-gray-gases model for the gaseous medium [5].

The viscous model was $k-\omega$ Shear Stress Transport (SST) for steady-state, which provided the initial condition for the transient calculations, where Scale Adaptive Simulation was used over the $k-\omega$ SST. NO_x emission was estimated by thermal and prompt pathways, calculated from the instantaneous N_2 , O_2 , OH, and O concentrations. The boundary conditions (BC) are summarized in Table 1.

Table 1. Boundary conditions.

Boundary	BC type	Case 1	Case 2
Atomization			
air inlet at 20 °C	Mass flow rate [g/s] ($\phi = 0.57$)	0.754 ($p_a = 0.75$ bar)	0.831 ($p_a = 0.9$ bar)
Combustion air inlet at 200 °C		7.04	6.97
Flue gas outlet	Pressure outlet [Pa]		0
Mixing tube and Combustion chamber wall	Heat transfer coefficient [W/m ² K] [33]	9.77 and 8.39	
	Ambient temperature [°C]	20	
	Emissivity [34]	0.5	
Other walls	Heat flux	0 (adiabatic)	
Fuel inlet ($\dot{Q} = 13.3$ kW)	Mass flow rate [g/s]	0.309	

2.3 Fuel properties

Physical material properties n-dodecane in both liquid and gaseous form were gathered mainly from the National Institute of Standards and Technology (NIST) database [35], modeled by polynomials. In the case of missing reference data for the evaluated temperature range,

estimation methods of ref. [36] were used. The required properties of liquid and gas phases and the used methods are listed in Table 2. The boiling point at normal conditions, $T_{b,n}$ of n-dodecane, was 489.3 K, which is close to 502.5 K, the initial boiling point of the measured diesel fuel sample used for the experiments. Latent heat of evaporation at $T_{b,n}$, $L_{T_{b,n}}$ of $C_{12}H_{26}$ was 256 kJ/kg, and the vapor pressure curve, p_{vs} , was determined by the Antoine equation. Liquid-phase density (ρ_l), specific heat capacity ($c_{p,l}$), dynamic viscosity (μ_l), and surface tension (σ) were available from 260 K up to T_{bn} from NIST or by calculation methods. The temperature interval for vapor-phase specific heat capacity ($c_{p,v}$) and mutual diffusion coefficient of vapor and air ($D_{v,a}$) ranged from 280 K to 2000 K, while dynamic viscosity (μ_v), thermal conductivity (k_v) of air and products were treated as constants since their variation was considered as small. The lower heating value of the diesel fuel was 43 MJ/kg, and the stoichiometric air-to-fuel ratio was 14.4 kg air/kg fuel.

Table 2. Material properties of n-dodecane, used for modeling diesel fuel.

diesel (n-C₁₂H₂₆)	
T_{bn}	NIST
$L_{T_{bn}}$	NIST
ρ_l	NIST
$c_{p,l}$	NIST
μ_l	NIST
σ	Brock [37]
$c_{p,v}$	Joback [38,39]
μ_v	Lucas [40]
k_v	Modified Eucken method [41]
$D_{v,a}$	Fuller [42,43]
p_v	NIST

3. Results and discussion

The comprehensive evaluation of the CFD results is presented in this section, which encompasses 0.1 s flow time, presenting both time-averaged and instantaneous data. The first subsection focuses on the chemical part to characterize the flame: temperature and OH distribution. It is followed by flow field and vortex structure evaluation in Subsections 3.2 and

3.3. In Subsection 3.4, NO_x formation was analyzed. Finally, the validation of the numerical results by Schlieren images is presented.

3.1 Temperature and OH distribution

The time-averaged temperature fields are shown in Fig. 4. The results of Cases 1 and 2 were similar; the difference is the increased cool atomizing air jet for Case 2. Both atomizing jets produce a notable cold air wake. The increased axial momentum, hence, decreasing swirl number (S), is clearly visible in Case 2 as the mixing tube outlet features the V-shape with a smaller angle. One characteristic feature of distributed combustion is the lifted flame, visible in both cases. Mind the log scale to allow the presentation of both cold air jet discharge and hot flue gas.

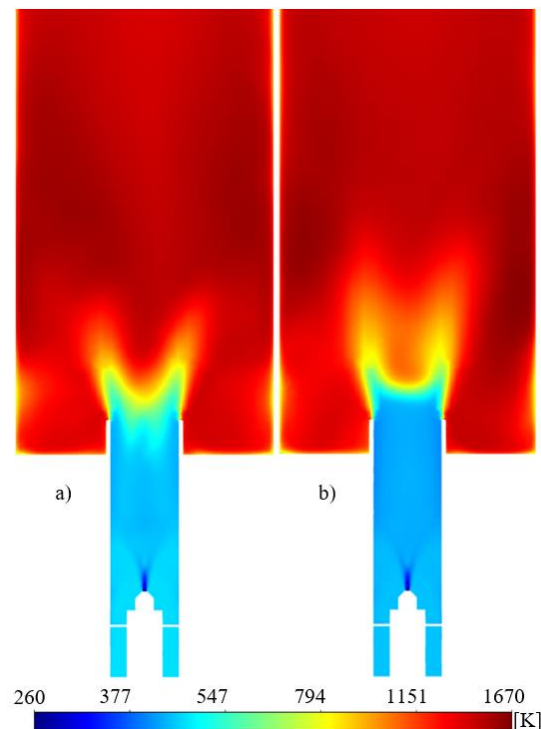


Fig. 4. Average temperature distribution of a) Case 1 and b) Case 2. Note the log scale.

The Root Mean Square (RMS) of the temperature is shown in Fig. 5. Generally, the mixing tube features notable oscillations arising from the fluctuating atomizing jet, otherwise, its temperature field is stable, including the hot flue gas part 100 mm downstream the mixing tube outlet. Since the axial momentum is smaller in Case 1, there is a strong fluctuation right above the mixing tube outlet as the mixture occasionally flashes backward, according to the simulation. Due to the increased axial momentum of Case 2, arising from $p_a = 0.9$ bar, the oscillations are present only downstream of the average ignition zone, shown in Fig. 5, with smaller and less-localized fluctuations. Due to the swirling flow, the fluctuations follow a V-shape. Its magnitude is higher in Case 1, as ignition occurs closer to the mixing tube outlet. Here, the fluctuations in the Outer Recirculation Zone (ORZ) are also higher.

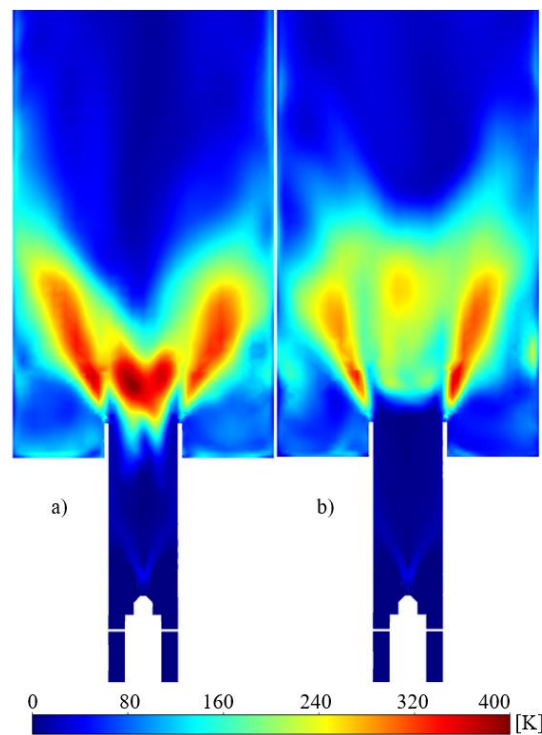


Fig. 5. RMS temperature distribution of a) Case 1 and b) Case 2.

Figure 6 shows the mean OH distribution, representing the heat release. Ignition occurs after the mixing tube and occupies a large, downstream part of the combustion chamber. The

heat release intensity is higher in Case 2, which correlates with the temperature distribution in Fig. 4b.

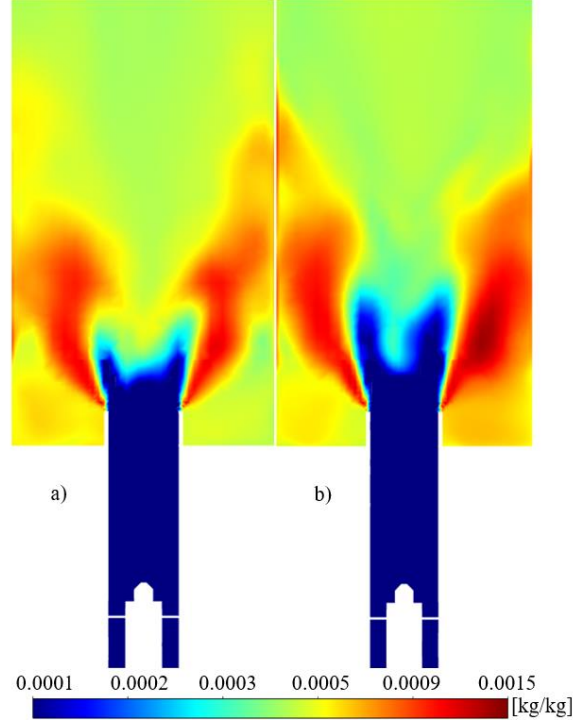


Fig. 6. Mean OH distribution of a) Case 1 and b) Case 2. Note the log scale.

3.2 Velocity distribution

Subsection 3.1 highlighted the two critical projections of the heat release: temperature and heat release distribution via OH. To better understand burner operation, hydrodynamic characteristics should be assessed, which is encompassed in Subsections 3.2 and 3.3. Figure 7 presents the mean velocity magnitude distribution. Since this is a swirl burner, the V shape in velocity magnitude is present. S is defined as [44]:

$$S = \frac{2\pi \int_0^R (Wr) \rho U r \, dr}{2\pi \int_0^R U \rho U r \, dr + 2\pi \int_0^R p r \, dr} \frac{1}{R}, \quad (1)$$

where R is the radius of the mixing tube, W is the tangential velocity, U is the axial velocity, p is the static pressure, ρ is the average density of the mixture, and r is the radial coordinate. The value of S is 0.33 for Case 1 and 0.27 for Case 2, calculated in the mixing tube, 20 mm downstream the atomization nozzle. The analytically estimated values were 0.25 and 0.22. Since S is lower in Case 2, this is inherited to the velocity distribution, meaning a less intense V-shape as the axial momentum of this flow is higher. Also, the velocity magnitude inside the V is higher and occupies a larger zone in Case 1. These results correlate well with the temperature fields presented in Fig. 4. Even though p_a is larger in Case 2, the difference is marginal; both atomizing jets decay fast. Their effects are confined to the first half of the mixing tube.

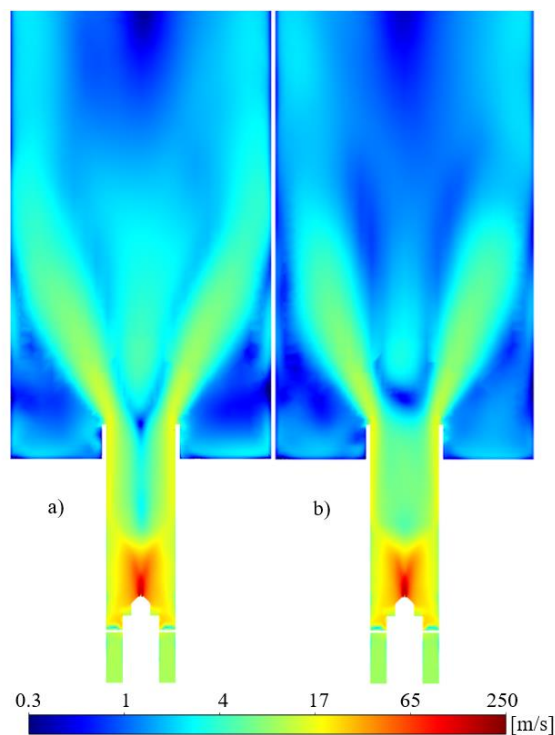


Fig. 7. Average velocity magnitude distribution of a) Case 1 and b) Case 2. Note the log scale.

Figure 8 shows the unsteady vortex formation in the V-shaped discharge, as it is known in the literature [6,45]. The atomizing jet leans to the wall, but not in the way as the mean plot

shows it. The instantaneous plots show that they lean to one side and rotate around, even in the case of geometric symmetry. The swirling flow finally entrains the jet, and the bulk flow is then pushed towards the walls. This is followed by the droplets, shown in Fig. 9a and b, since their size, hence, their momentum is small. The mean evaporated fuel concentration is presented in Fig. 9c and d, indicating that the mean is symmetrical, and the highest concentration can be found near the walls. The reason for this is that the droplets need time to evaporate fully, which is most dominant in the region where the atomizing jet was attached to the wall. The fuel is present only up to the flame zone, making a perfect match with the low-temperature zone of Fig. 4. The faster evaporation in Case 2 is also attributed to the smaller droplet sizes by the increased p_a .

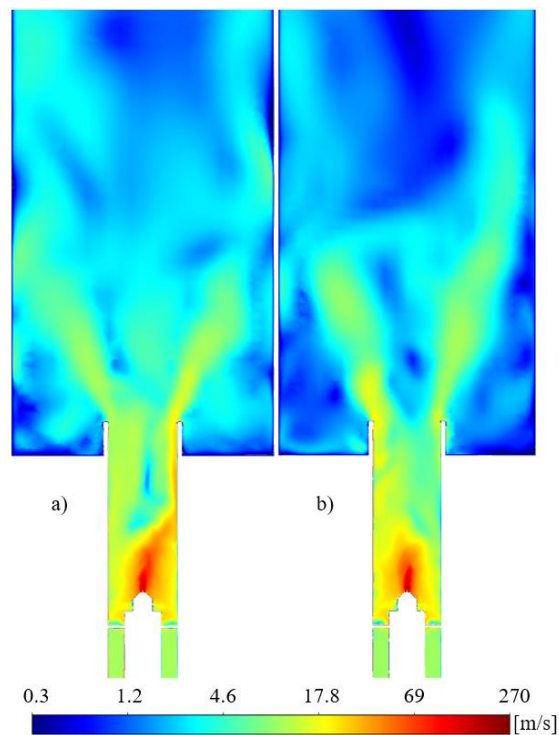


Fig. 8. Instantaneous velocity distribution of a) Case 1 and b) Case 2. Note the log scale.

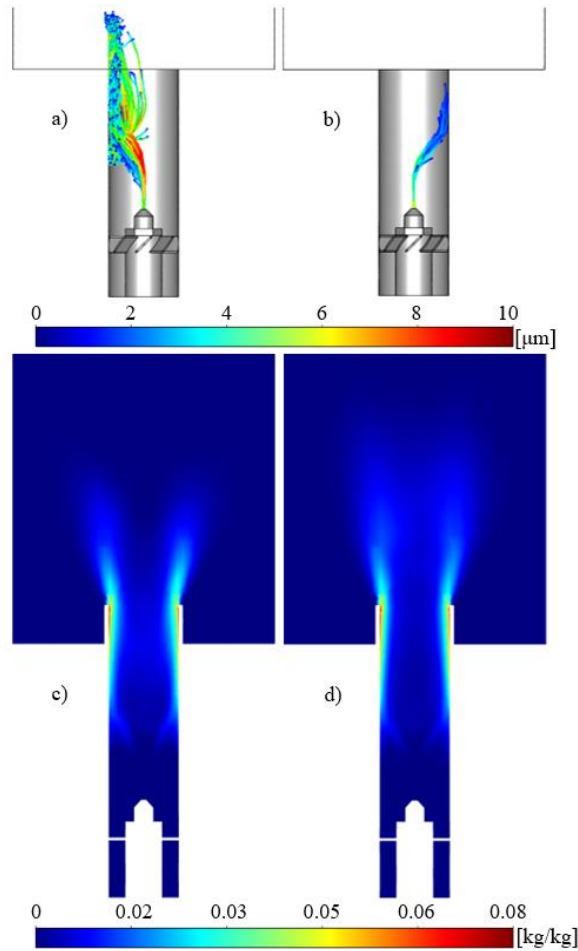


Fig. 9. Droplet pathways in the Lagrangian frame of a) Case 1 and b) Case 2 and mean dodecane distribution of c) Case 1 and d) Case 2.

Turbulence intensity describes the fluctuations compared to the mean flow, shown in Fig. 10. Its value is extremely high in the mixing tube due to all atomization, unsteady atomizing jet, and the intense swirling flow. Turbulence is intense in the reaction zone as the gas temperature increases, but free expansion is not allowed. Finally, it decays in the post-flame zone.

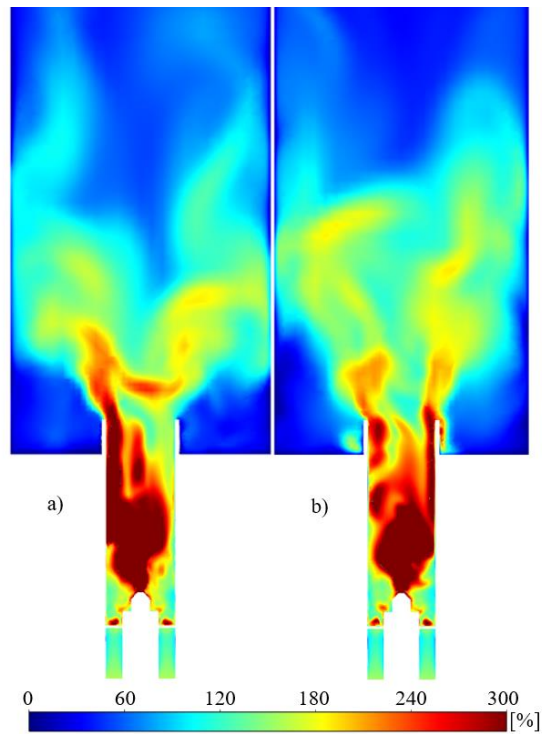


Fig. 9. Instantaneous turbulence intensity in a) Case 1 and b) Case 2.

3.3 Vortex structures

Figure 10 shows the Internal Recirculation Zone (IRZ) by vector plots, colored by the mean OH concentration, which indicated a lifted flame. The ORZ is relatively weak and features a high variation since its structure is poorly localized in the mean vector plot. Downstream of the IRZ, there is a notable scatter in the vector field, referring to small but frequently appearing vortices.

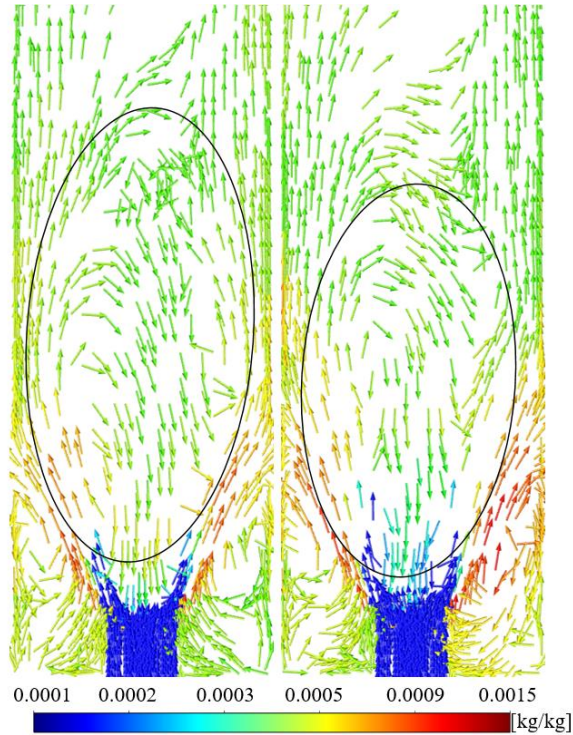


Fig. 10. Mean velocity vector field colored by mean OH concentration in a) Case 1 and b) Case 2. Note the log scale.

To visualize the vortical structures, the λ_2 criterion was used, and the result is shown in Fig. 11, colored by temperature. Two dominant toroidal vortices are present in the combustion chamber in Case 2. Their high and even temperature field represent distributed combustion. The excellent stability near blowout [14] is supported by the several additional large vortical structures, which are not coherent with the two toroidal ones, facilitating ignition even when the large structures are shrinking or leaving the reaction zone. IRZ also acts as a key component of combustion stabilization, countering flame blowout. A precessing vortex core was identified in both cases, however, the higher atomization pressure blew it out in Case 2. Corner vortices are present with lower temperatures and less regular shape than in the case of classical ORZ of swirl burners [46,47]. The randomness of the vortex structure is the key to all flame stabilization under lean conditions, reduced volumetric HRR, and low acoustic noise.

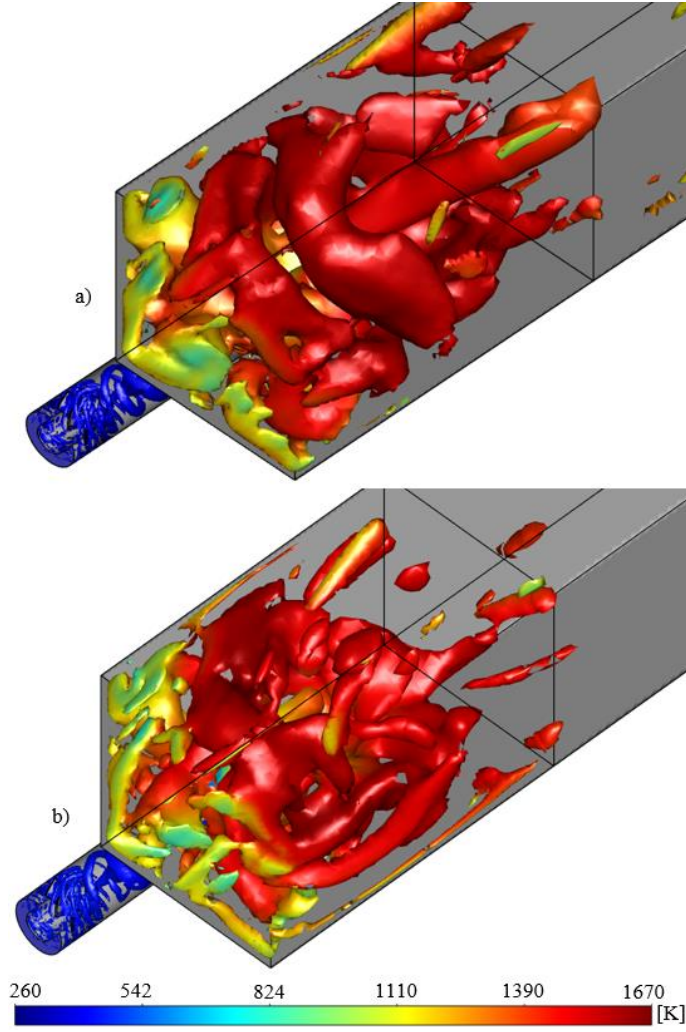


Fig. 11. Mean vortex structures at $\lambda_2 = -750 \text{ 1/s}^2$ colored by temperature. a) Case 1 and b) Case 2.

A critical question of distributed combustion and the associated unnecessary exhaust gas recirculation or oxidizer dilution by inert gas of the MTC burner is the extent of internal flue gas recirculation. There are combustion chambers building around this phenomenon [48,49] since intense internal recirculation zones decrease the volumetric HRR. The other possibility of reduced HRR is the lack of internal recirculation, but the flame speed decreases due to the unique flow structures. To address this question, the reactant dilution ratio, the extent of the recirculation of burnt species to the fresh mixture, can be calculated as [50]:

$$R_{dil} = \frac{|\dot{m}_{ax}| - (\dot{m}_{air} + \dot{m}_{fuel})}{\dot{m}_{air} + \dot{m}_{fuel}}, \quad (2)$$

where \dot{m}_{air} , \dot{m}_{fuel} are the mass flow rate of the total inlet air and the fuel, and $\dot{m}_{ax} = \iint \rho v_{ax} dx dy$ is the backflow mass flow rate. The instantaneous results are shown in Fig. 12 along the axial direction of the combustion chamber.

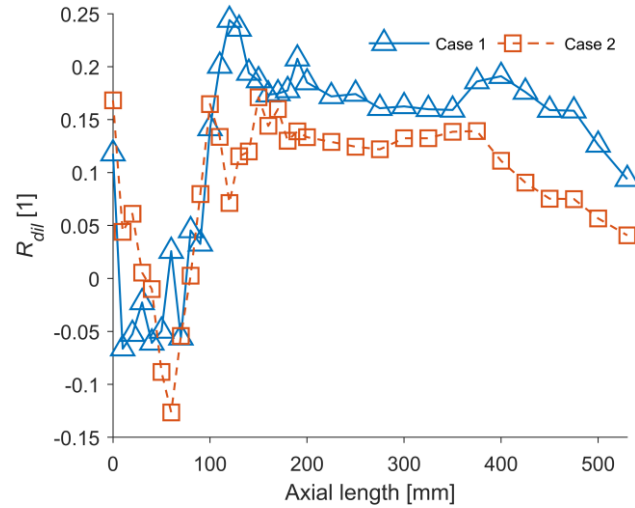


Fig. 12. Reactant dilution ratio in the combustion chamber along the axis. The origin is the bottom of the combustion chamber.

It can be concluded that recirculation is negligible, up to 100 mm. Then both IRZ and ORZ affect the flow. The small but negative values can be explained by the intermittent flow behavior arising from evaluating the instantaneous results. Since the vortical structures, which transfer flue gas back, are not confined to the reaction zone, their presence in the latter part of the combustion chamber is still significant, and they start to break up after 300 mm. For comparison, refs. [50] and [51] show an order of magnitude higher R_{dil} to achieve low-emission combustion. In conclusion, the MTC burner achieves distributed combustion principally by cooling the reactants while maintaining a rather random flow field instead of relying on exhaust gas recirculation.

3.4 NO_x emission

Figure 15 shows the time-averaged NO_x distribution. The mass-weighted average values on the combustion chamber outlet were below 1 ppm at 15% O_2 , agreeing with the measured values, which were 2.5 and 2 ppm for Cases 1 and 2 with 1 ppm uncertainty [14]. Since the flame temperature was peaking at 1670 K, the thermal NO_x production is already low in the post-flame region. Instead, prompt NO_x production can be identified in the computational domain, which stays low due to the lean conditions. The combined effect of the two ultimately leads to ultra-low emissions.

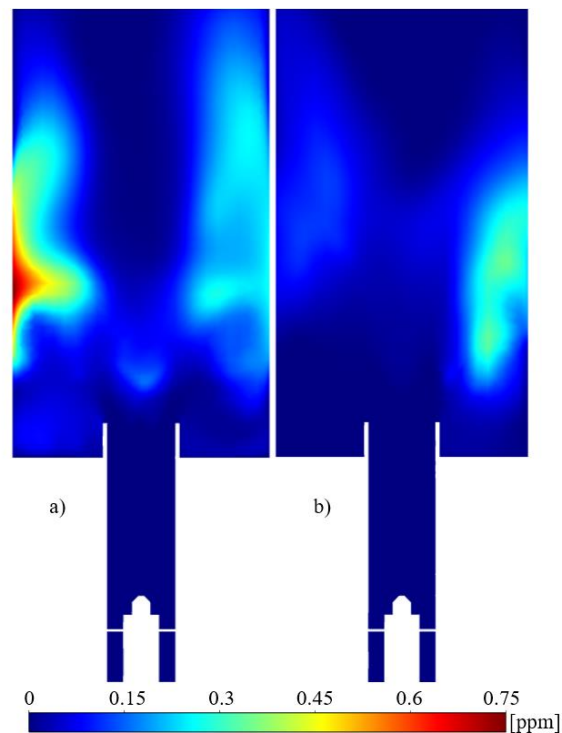


Fig. 15. Mean NO_x distribution at 15% O_2 , a) Case 1 and b) Case 2.

3.5 Validation

The Schlieren setup was focused on an 86×86 mm central field, including the mixing tube outlet. Hence, the numerical results were focused on this area. Figure 13 shows the RMS densities, based on 0.2 s real time of 2000 images at 10 kHz sampling frequency, while that of

CFD analysis was 0.1 s, using 10,000 calculation steps. Higher values are present at the lip of the mixing tube on both the measurement and numerical data. The CFD results show a more symmetric distribution, while the Schlieren images are asymmetric, hence, the Abel transform was not applied here. However, it can be concluded that the density fluctuation is more intense at the combustion chamber inlet because of the intense mixing. Similar to Case 1, Case 2 presents high-density variation near the mixing tube outlet in Fig. 13.

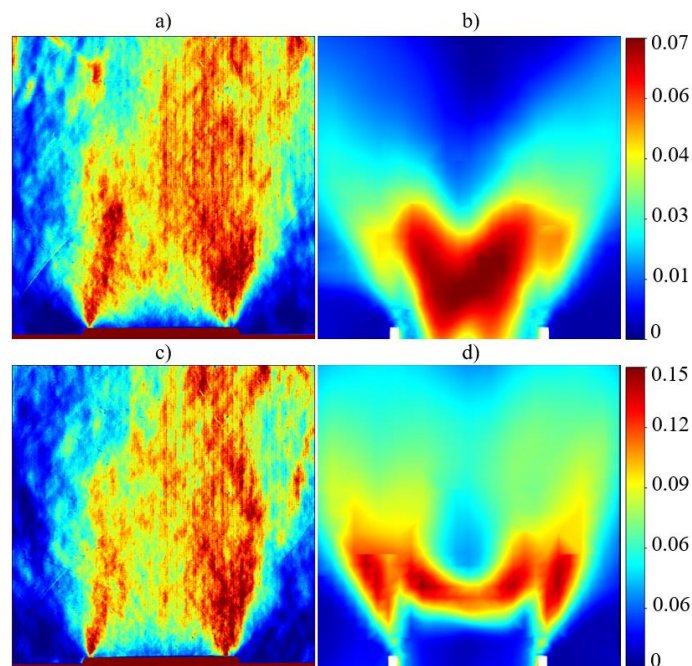


Fig. 13. Schlieren RMS image of a) Case 1 and b) Case 2 and RMS density [kg/m^3] of CFD analysis of b) Case 1 and d) Case 2.

Figure 14 shows the comparison of raw instantaneous Schlieren images and OH distribution. The small, characteristic cellular structures on the Schlieren images show the cold eddies containing the fuel-air mixture. Their boundary indicates ignition, which was also tracked by the appearing OH concentration in the CFD analysis. The increased p_a leads to deeper penetration of the cold jet into the combustion chamber.

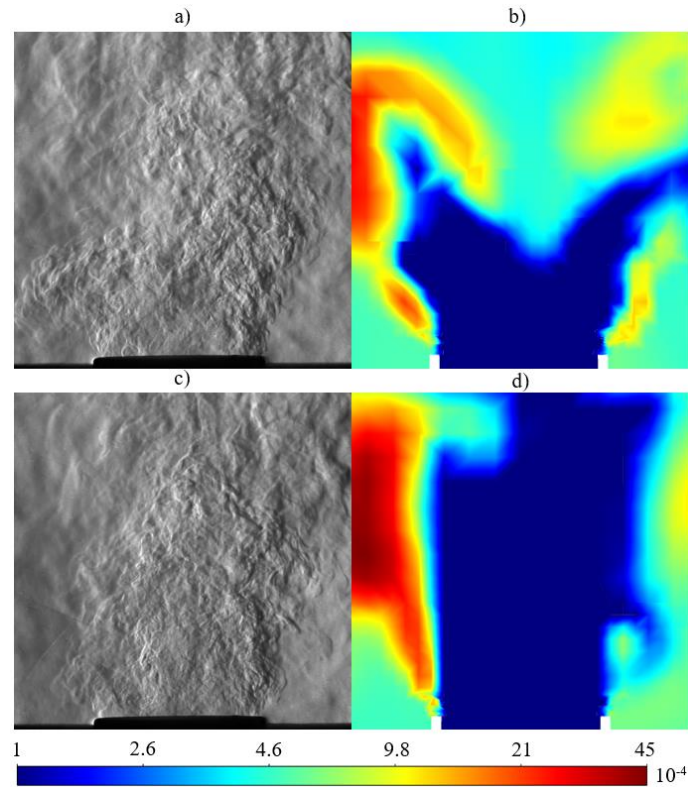


Fig. 14. Raw instantaneous Schlieren images of a) Case 1 and b) Case 2 and instantaneous volumetric OH concentration of the CFD analysis of c) Case 1 and d) Case 2. Note the log scale.

4. Conclusions

This paper numerically investigated two distributed combustion setups in ANSYS Fluent software environment. Diesel fuel combustion was modeled by FGM with notably reduced turbulent flame speed coefficients in the Zimont model to achieve the observed flame. The results were validated by Schlieren images, comparing the RMS densities and OH with the boundaries of the cold fuel-air mixture. The agreement between experiments and simulation results is notably better than in the case of several recent papers on distributed combustion, probably due to their overestimated turbulent flame speed.

RMS temperature and OH distribution revealed the intense reaction zone and its fluctuations, lifted from the burner outlet. The flame shapes differ from V, however, mean velocity magnitude shows a dominant V shape since a swirl burner was investigated with 45°

axial vanes. The vortex structures showed that large vortices develop in the upper section of the combustion chamber, while their distributions are rather amorphous. The reactant dilution ratio was calculated to check the extent of inner recirculation. Although the vector field and the vortex structure showed large backflow areas, the instantaneous recirculation is insignificant compared to EGR of MILD combustion or systems building around inner EGR.

The reason for the ultra-low NO_x formation is the low and homogenous post-flame temperature, also affected by the highly lean conditions. Hence, the thermal pathway is hindered, and also negligible prompt NO formation was found. The simulated emissions were below 1 ppm, while that of the experiments was 2.5 and 2 ppm for the two cases.

Funding

The research reported in this paper was supported by the National Research, Development and Innovation Fund of Hungary, project №.s OTKA-FK 124704, 134277, 137758 and TKP2020 NC, Grant No. BME-NC, based on the charter of bolster issued by the NRD Office under the auspices of the Ministry for Innovation and Technology. The support of the project “Computer Simulations for Effective Low-Emission Energy Engineering” funded as project No. CZ.02.1.01/0.0/0.0/16_026/0008392 by Operational Programme Research, Development and Education, Priority axis 1: Strengthening capacity for high-quality research.

Conflict of interest

The authors declare that there is no conflict of interest.

References

- [1] Hannula I, Reiner DM. Near-Term Potential of Biofuels, Electrofuels, and Battery Electric Vehicles in Decarbonizing Road Transport. *Joule* 2019;3:2390–402.

- doi:10.1016/j.joule.2019.08.013.
- [2] Pan X, Wang H, Wang L, Chen W. Decarbonization of China's transportation sector: In light of national mitigation toward the Paris Agreement goals. *Energy* 2018;155:853–64. doi:10.1016/j.energy.2018.04.144.
 - [3] IEA. Transport: Improving the sustainability of passenger and freight transport 2020.
 - [4] European Commission. Sustainable aviation fuels – ReFuelEU Aviation 2021.
 - [5] Liu Y, Sun X, Sethi V, Nalianda D, Li YG, Wang L. Review of modern low emissions combustion technologies for aero gas turbine engines. *Prog Aerosp Sci* 2017;94:12–45. doi:10.1016/j.paerosci.2017.08.001.
 - [6] Huang Y, Yang V. Dynamics and stability of lean-premixed swirl-stabilized combustion. *Prog Energy Combust Sci* 2009;35:293–364. doi:10.1016/j.pecs.2009.01.002.
 - [7] Lefebvre AH, Ballal DR. Gas turbine combustion. third. Boca Raton: CRC Press; 2010. doi:10.1002/1521-3773.
 - [8] Sobhani S, Muhunthan P, Boigné E, Mohaddes D, Ihme M. Experimental feasibility of tailored porous media burners enabled via additive manufacturing. *Proc Combust Inst* 2021;38:6713–22. doi:10.1016/j.proci.2020.06.120.
 - [9] Xing F, Kumar A, Huang Y, Chan S, Ruan C, Gu S, et al. Flameless combustion with liquid fuel: A review focusing on fundamentals and gas turbine application. *Appl Energy* 2017;193:28–51. doi:10.1016/j.apenergy.2017.02.010.
 - [10] Reddy VM, Sawant D, Trivedi D, Kumar S. Studies on a liquid fuel based two stage flameless combustor. *Proc Combust Inst* 2013;34:3319–26. doi:10.1016/j.proci.2012.06.028.
 - [11] Khalil AEE, Gupta AK. Towards colorless distributed combustion regime. *Fuel* 2017;195:113–22. doi:10.1016/j.fuel.2016.12.093.
 - [12] J. A. Wüning and J. G. Wüning. Flameless oxidation to reduce thermal NO-formation. *Prog Energy ComlnaL Sci* 1997;23:81–94.
 - [13] Karyeyen S, Feser JS, Jahoda E, Gupta AK. Development of distributed combustion index from a swirl-assisted burner. *Appl Energy* 2020;268:114967. doi:10.1016/j.apenergy.2020.114967.
 - [14] Józsa V. Mixture temperature-controlled combustion: A revolutionary concept for ultra-low NO_x emission. *Fuel* 2021;291:120200. doi:10.1016/j.fuel.2021.120200.
 - [15] Füzesi D, Cheng Tung C, Józsa V. Numerical modeling of waste cooking oil biodiesel combustion in a turbulent swirl burner. 10th Eur. Combust. Meet. Proc., Naples: 2021, p. 397–402.
 - [16] van Oijen JA, Donini A, Bastiaans RJM, ten Thijsse Boonkamp JHM, de Goey LPH. State-of-the-art in premixed combustion modeling using flamelet generated manifolds. *Prog Energy Combust Sci* 2016;57:30–74. doi:10.1016/j.pecs.2016.07.001.
 - [17] Kuti OA, Sarathy SM, Nishida K. Spray combustion simulation study of waste cooking oil biodiesel and diesel under direct injection diesel engine conditions. *Fuel* 2020;267:117240. doi:10.1016/j.fuel.2020.117240.
 - [18] Cerinski D, Vujanović M, Petranović Z, Baleta J, Samec N. Numerical analysis of fuel injection configuration on nitrogen oxides formation in a jet engine combustion chamber. *Energy Convers Manag* 2020;220:112862. doi:10.1016/j.enconman.2020.112862.
 - [19] Ilbas M, Kumuk O, Karyeyen S. Modelling of the gas-turbine colorless distributed combustion: An application to hydrogen enriched e kerosene fuel. *Int J Hydrogen Energy* 2021. doi:10.1016/j.ijhydene.2021.06.228.
 - [20] Ilbas A, Bahadır M, Karyeyen S. Investigation of colorless distributed combustion regime using a high internal recirculative combustor. *Int J Hydrogen Energy* 2021.

- doi:10.1016/j.ijhydene.2021.05.209.
- [21] Dixit S, Kumar A, Kumar S, Waghmare N, Thaku HC, Khan S. CFD analysis of biodiesel blends and combustion using Ansys Fluent. *Mater Today Proc* 2019;26:665–70. doi:10.1016/j.matpr.2019.12.362.
- [22] Tu Y, Xu M, Zhou D, Wang Q, Yang W, Liu H. CFD and kinetic modelling study of methane MILD combustion in O₂/N₂, O₂/CO₂ and O₂/H₂O atmospheres. *Appl Energy* 2019;240:1003–13. doi:10.1016/j.apenergy.2019.02.046.
- [23] Abdulrahman H, Validi A, Jaber F. Large-eddy simulation/filtered mass density function of non-premixed and premixed colorless distributed combustion Large-eddy simulation/ filtered mass density function of non-premixed and premixed colorless distributed combustion 2021;055118. doi:10.1063/5.0045904.
- [24] Arghode VK, Gupta AK, Bryden KM. High intensity colorless distributed combustion for ultra low emissions and enhanced performance. *Appl Energy* 2012;92:822–30. doi:10.1016/j.apenergy.2011.08.039.
- [25] ANSYS Inc. 5 Best Practices for Gas Turbine Combustion Meshing Using Ansys Fluent. Canonsburg: 2020.
- [26] Lefebvre AH, McDonell VG. *Atomization and Sprays*. Second. Boca Raton, FL, FL: CRC Press; 2017.
- [27] Urbán A, Katona B, Malý M, Jedelský J, Józsa V. Empirical correlation for spray half cone angle in plain-jet airblast atomizers. *Fuel* 2020;277:118197. doi:10.1016/j.fuel.2020.118197.
- [28] ANSYS Inc. ANSYS Fluent Theory Guide. Release 2020 R1. Canonsburg: 2020.
- [29] Savard B, Wang H, Wehrfritz A, Hawkes ER. Direct numerical simulations of rich premixed turbulent n-dodecane/air flames at diesel engine conditions. *Proc Combust Inst* 2019;37:4655–62. doi:https://doi.org/10.1016/j.proci.2018.08.022.
- [30] E. Ranzi, A. Frassoldati, A. Stagni, M. Pelucchi, A. Cuoci TF. Reduced Kinetic Schemes of Complex Reaction Systems: Fossil and Biomass-Derived Transportation Fuels. *Int J Chem Kinet* 2014;46(9):512–542.
- [31] Zhang K, Ghobadian A, Nouri JM. Comparative study of non-premixed and partially-premixed combustion simulations in a realistic Tay model combustor. *Appl Therm Eng* 2017;110:910–20. doi:10.1016/j.applthermaleng.2016.08.223.
- [32] Chong CT, Hochgreb S. Measurements of laminar flame speeds of liquid fuels : Jet-A1, diesel, palm methyl esters and blends using particle imaging velocimetry (PIV). *Proc Combust Inst* 2011;33:979–86. doi:10.1016/j.proci.2010.05.106.
- [33] Martin M, Holge K, editors. *VDI Heat Atlas*. 2nd ed. Berlin, Heidelberg: Springer-Verlag Berlin Heidelberg; 2010.
- [34] Technologies L. *Table of emissivity of various surfaces*. Schaffhausen: Mikron Instrument Company, Inc.; 2003.
- [35] Lemmon EW, McLinden MO, Friend DG. *Thermophysical Properties of Fluid Systems, NIST Chemistry WebBook, NIST Standard Reference Database Number 69* n.d. doi:doi:10.18434/T4D303.
- [36] Csemány D, Gujás I, Chong CT, Józsa V. Evaluation of material property estimating methods for n-alkanes, 1-alcohols, and methyl esters for droplet evaporation calculations. *Heat Mass Transf* 2021. doi:10.1007/s00231-021-03059-0.
- [37] Brock JR, Bird RB. Surface tension and the principle of corresponding states. *AIChE J* 1955;1:174–7. doi:https://doi.org/10.1002/aic.690010208.
- [38] Joback KG. *A Unified Approach to Physical Property Estimation Using Multivariate Statistical Techniques*. Massachusetts Institute of Technology, Department of Chemical Engineering; 1984.
- [39] Joback KG, Reid RC. Estimation of pure-component properties from group-

- contributions. *Chem Eng Commun* 1987;57:233–43. doi:10.1080/00986448708960487.
- [40] Lucas K. Die Druckabhängigkeit der Viskosität von Flüssigkeiten – eine einfache Abschätzung. *Chemie Ing Tech* 1981;53:959–60. doi:10.1002/cite.330531209.
- [41] Svehla RA. Estimated Viscosities and Thermal Conductivities of Gases at High Temperatures. Cleveland, Ohio: NASA Tech. Rept. R-132, Lewis Research Center; 1962.
- [42] Fuller EN, Schettler PD, Giddings JC. New method for prediction of binary gas-phase diffusion coefficients. *Ind Eng Chem* 1966;58:18–27. doi:10.1021/ie50677a007.
- [43] Fuller EN, Ensley K, Giddings JC. Diffusion of halogenated hydrocarbons in helium. The effect of structure on collision cross sections. *J Phys Chem* 1969;73:3679–85. doi:10.1021/j100845a020.
- [44] Beér JM, Chigier NA. *Combustion aerodynamics*. London: Robert E. Krieger Publishing Company, Inc.; 1972.
- [45] Taamallah S, Dagan Y, Chakroun N, Shanbhogue SJ, Vogiatzaki K, Ghoniem AF. Helical vortex core dynamics and flame interaction in turbulent premixed swirl combustion : A combined experimental and large eddy simulation investigation Helical vortex core dynamics and flame interaction in turbulent premixed swirl combustion : A combi. *Phys Fluids* 2019;31:025108. doi:10.1063/1.5065508.
- [46] Mansouri Z, Aouissi M, Boushaki T. A numerical study of swirl effects on the flow and flame dynamics in a lean premixed combustor. *Int J Heat Technol* 2016;34:227–35. doi:10.18280/ijht.340211.
- [47] Elorf A, Sarh B, Tabet F, Bostyn S, Asbik M, Bonnamy S, et al. Effect of Swirl Strength on the Flow and Combustion Characteristics of Pulverized Biomass Flames. *Combust Sci Technol* 2019;191:629–44. doi:10.1080/00102202.2018.1497611.
- [48] Sharma S, Chowdhury A, Kumar S. A novel air injection scheme to achieve MILD combustion in a can-type gas turbine combustor. *Energy* 2020;194:116819. doi:10.1016/j.energy.2019.116819.
- [49] Sharma S, Kumar R, Chowdhury A, Yoon Y, Kumar S. On the effect of spray parameters on CO and NO_x emissions in a liquid fuel fired flameless combustor. *Fuel* 2017;199:229–38. doi:10.1016/j.fuel.2017.02.102.
- [50] Sharma S, Singh P, Gupta A, Chowdhury A. Distributed combustion mode in a can-type gas turbine combustor – A numerical and experimental study. *Appl Energy* 2020;277:115573. doi:10.1016/j.apenergy.2020.115573.
- [51] Kumar S, Paul PJ, Mukunda HS. Studies on a new high-intensity low-emission burner 2002;29:1131–7.